



Exceeding the classical time-bandwidth product in nonlinear time-invariant systems

Alireza Mojahed · Kosmas L. Tsakmakidis · Lawrence A. Bergman · Alexander F. Vakakis

Received: 25 August 2021 / Accepted: 1 April 2022
© The Author(s), under exclusive licence to Springer Nature B.V. 2022

Abstract The classical “time-bandwidth” limit for linear time-invariant (LTI) devices in physics and engineering asserts that it is impossible to store broadband propagating waves (large $\Delta\omega$'s) for long times (large Δt 's). For standing (non-propagating) waves, i.e., vibrations, in particular, this limit takes on a simple form, $\Delta t \Delta\omega = 1$, where $\Delta\omega$ is the bandwidth over which localization (energy storage) occurs, and Δt is the storage time. This is related to a well-known result in dynamics, namely that one can achieve a high Q-factor (narrowband resonance) for low damping, or small Q-factor (broadband resonance) for high

damping, but not simultaneously both. It thus remains a fundamental challenge in classical wave physics and vibration engineering to try to find ways to overcome this limit, not least because that would allow for storing *broadband* waves for *long* times, or achieving broadband resonance for low damping. Recent theoretical studies have suggested that such a feat might be possible in LTI terminated unidirectional waveguides or LTI topological “rainbow trapping” devices, although an experimental confirmation of either concept is still lacking. In this work, we consider a nonlinear but time-invariant mechanical system and demonstrate experimentally that its time-bandwidth product can exceed the classical time-bandwidth limit, thus achieving values both above and below unity, in an energy-tunable way. Our proposed structure consists of a single-degree-of-freedom nonlinear oscillator, rigidly coupled to a nondispersive waveguide. Upon developing the full theoretical framework for this class of nonlinear systems, we show how one may control the nonlinear flow of energy in the frequency domain, thereby managing to disproportionately decrease (increase) Δt , the storage time in the resonator, as compared with an increase (decrease) of the system's bandwidth $\Delta\omega$. Our results pave the way toward conceiving and harnessing hitherto unattainable broadband and simultaneously low-loss wave-storage devices, both linear and nonlinear, for a host of key applications in wave physics and engineering.

Alireza Mojahed and Kosmas L. Tsakmakidis have contributed equally in preparing this article.

A. Mojahed (✉) · A. F. Vakakis
Department of Mechanical Science and Engineering,
University of Illinois, Urbana, IL 61801, USA
e-mail: mojahed2@illinois.edu

Present Address:
A. Mojahed
Massachusetts Institute of Technology, Cambridge,
MA 02139, USA

K. L. Tsakmakidis
Section of Condensed Matter Physics, Department of
Physics, National and Kapodistrian University of Athens,
Panepistimioupolis, GR-157 84 Athens, Greece

L. A. Bergman
Department of Aerospace Engineering, University of
Illinois, Urbana, IL 61801, USA

Keywords Nonlinear bandwidth · Time-bandwidth product

1 Introduction and preliminaries

Take any linear time-invariant (LTI) resonant device storing (localizing) for a certain amount of time a wave of amplitude x inside it—this can range [1] from a microcavity in silicon photonics, a meta-atom (e.g., split-ring resonator) in metamaterials, or a metallic/dielectric particle in (nano) plasmonics, to a resonator in a mechanical/acoustic system or in cavity quantum electrodynamics/opto-mechanics. Such systems are currently being used in an extremely broad range of applications [1–15] in physics and engineering, from ultrasensitive sensors to on-chip frequency combs, and from ultrafast nanolasers to resonant “meta-atoms” in metamaterials deployed for subwavelength imaging, high-speed modulation, invisibility cloaking, and light slowing/stopping. Moreover, the use of resonators is universal across scales in diverse engineering fields.

Inside this resonant system, a standing wave (or vibration) will oscillate sinusoidally, say with a frequency ω_0 , and will decay with time owing to some loss mechanism(s) with a (total) decay rate λ , i.e., it will satisfy [1] $x(t) \propto \cos(\omega_0 t) \times e^{-(1/2)\lambda t}$. Hence, in the resonance approximation and in the usual underdamped regime ($\lambda/2 \ll \omega_0$), the intensity of the vibration will be given by,

$$E(\omega) = \frac{1}{(\lambda/2)^2 + \omega^2}, \quad (1)$$

where in the frequency domain, the energy spectral density is defined as $E(\omega) = |\mathcal{F}\{\dot{x}\}|^2$ with $(\dot{\cdot})$ indicating the operator extracting the envelope of its argument and \mathcal{F} denoting the Fourier transform operator. From relation (1), it is immediately seen that the (classical half-amplitude) bandwidth is $\Delta\omega = \lambda$; in other words, the product of the storage time, $\Delta t = 1/\lambda$, with $\Delta\omega$ appears to always be equal to unity, $\Delta t \Delta\omega = 1$, and this holds for any single-degree-of-freedom lightly damped linear time-invariant resonator. This limit is known as the classical “time-bandwidth (T-B) limit” [1, 9, 11, 16, 17] of LTI resonant devices.

The classical T–B limit ($\Delta t \Delta\omega = 1$) has never been violated in any LTI resonant or wave-localizing structure [1, 9, 11], including (but not limited to) such broad areas of research as optical microcavities, metamaterial or dielectric resonant structures, (nano)-plasmonics, and Anderson localization of waves—remaining a long-sought-after fundamental objective in wave physics and engineering to do so. Achieving T–B products above unity would, e.g., imply that we could harness the “best of both worlds” in the above systems, namely storing waves for, simultaneously, long times *and* broad bandwidths. Conversely, tuning this limit *below* unity would mean that, e.g., for a fixed large bandwidth, the release of a wave excitation would be faster than what is normally allowed (for that bandwidth); again, this would find a range of important technological applications, such as energy harvesting [3], vibration absorption and isolation [12], and the attainment of on-chip nonreciprocity [7, 13].

It is therefore intriguing to inquire about what happens when only the ‘ L ’ (linearity) assumption is removed, i.e., when a system becomes nonlinear but remains time-invariant. From the start, however, we immediately recognize that in the nonlinear case, the notion of bandwidth is not readily available, so in order to study the time-bandwidth product of such a nonlinear time-invariant (NTI) resonator, we should first appropriately define its “nonlinear bandwidth.” We show in the following that for a general class of dynamical nonlinear (e.g., communication [18]) systems, this task can be achieved by considering the “root mean square (RMS) bandwidth” of the system. A detailed discussion of the nonlinear bandwidth definition is left for another work, and here, we only provide a brief exposition upon which our later results will be based.

In the following, we begin with providing an alternative and generalized definition of the classical bandwidth for dynamical systems that not only is valid for LTI systems and identical to the already-established bandwidth definition, e.g., half-power bandwidth, but also can be applied to nonlinear time-invariant systems. This is then followed by experimentally examining the time-bandwidth properties of a nonlinear dynamical system in scenarios where the nonlinearity is weak (negligible), strong, and of hardening or softening nature.

2 Generalization of bandwidth definition

To this end, we note that extending the concept of bandwidth for general classes of dynamical systems requires a formulation that is valid not only for low-loss LTI systems (for which the classical definition applies) but also encompasses systems with more general features, e.g., moderate or even high dissipative rates, time variant properties, and nonlinearities. Hence, we begin by acknowledging the fact that the bandwidth of a dynamical system (as in the traditional classical half-amplitude, also known as half-power, bandwidth definition) is one of its inherent properties and relates to its energy ($E(\omega)$) dissipation capacity (loss rate). For instance, in the case of a SDOF LTI resonator, a larger bandwidth, i.e., larger energy dispersion in the frequency domain, translates to faster energy dissipation, hence to higher time-locality of the energy signal. This means that, for example, in an acoustic setting, a larger bandwidth resonator connected to an acoustic waveguide releases its stored energy in the form of time localized (broadband) waves at a faster rate to the waveguide; conversely, a smaller bandwidth resonator releases its stored energy to the waveguide in the form of narrowband waves at a slower rate. The aforementioned temporal-localization is quantified by the well-known (half-amplitude) definition of bandwidth in linear time-invariant systems which considers the frequency response function, i.e., the Fourier transform of the free (impulse) response, of the system. For a low-loss linear system, this quantity is equal to its overall dissipative capacity—in this case, typically the viscous damping coefficient.

The time-locality of a signal can be quantified by its temporal variance, σ_t^2 , while its frequency dispersion can be quantified by its frequency-domain variance, σ_ω^2 . As is well established, these two quantities are related through the Fourier uncertainty principle [19], which states that for a signal (satisfying the Fourier-transformation requirements) the value of $\sigma_t^2 \sigma_\omega^2 = C \geq 1/16\pi^2$, where C is a constant. With the inverse proportionality of σ_t^2 and σ_ω^2 established, we now note that σ_ω^2 is, e.g., in standard communication systems [18], also known as $(\Delta\omega_{\text{rms}})^2$ —the aforementioned RMS bandwidth [2]. With this (RMS) bandwidth formula and its inverse relation to the time-locality of the signal, we can now compute the bandwidth of

broader classes of dynamical systems, such as both single- and multi-degree-of-freedom linear, time variant or invariant, as well as nonlinear dynamical systems. Indeed, one more argument that this general RMS bandwidth definition is the appropriate one is that for the energy spectrum $E(\omega)$ of the signal in Eq. (1), the RMS bandwidth given by,

$$\Delta\omega_{\text{rms}} \equiv \Delta\omega = 2\sqrt{\frac{\int_{-\infty}^{\infty} \omega^2 E^2(\omega) d\omega}{\int_{-\infty}^{\infty} E^2(\omega) d\omega}}, \quad (2)$$

leads, by a simple substitution of Eqs. (1–2), to the correct result for a linear SDOF system, that is, $\Delta\omega^* = \lambda$ —as it should, where the superscript (*) is used to denote the classical bandwidth definition. We emphasize here that since $\Delta\omega$ in (2) quantifies the overall *energy* dissipation rate of a system, the argument on the right-hand side contains $E^2(\omega)$ —and not other powers of $E(\omega)$ since these do not represent any physical feature(s) of the system. In order to use (2), one needs to compute the *energy* of the system/signal which typically requires an accurate mathematical model of the system, especially if the considered system is being examined experimentally. In order to alleviate this issue one may consider the envelope of its kinetic energy [20], which is sufficient given that the kinetic energy is proportional to the velocity-squared of the system (factored by the “mass” of the system); clearly, measuring the envelope of the velocity time series is always possible in both simulations and experiments. Owing to the fact that the envelope of the velocity corresponding to the free response of a nonlinear system is monotonically decaying and does not possess any non-stationary frequencies, its Fourier transform can be computed and used to compute the bandwidth of the system. In the next sections, we first introduce the system of interest in this study and then use the generalized bandwidth definition to show how a nonlinearity affects the time-bandwidth properties of an otherwise time-invariant system.

3 Experimental fixture and system identification

Based on the previous nonlinear bandwidth concept, we aim to experimentally demonstrate that the T–B product of a NTI mechanical system can be *tuned*—both *above* and, even more intriguingly, *below* unity—

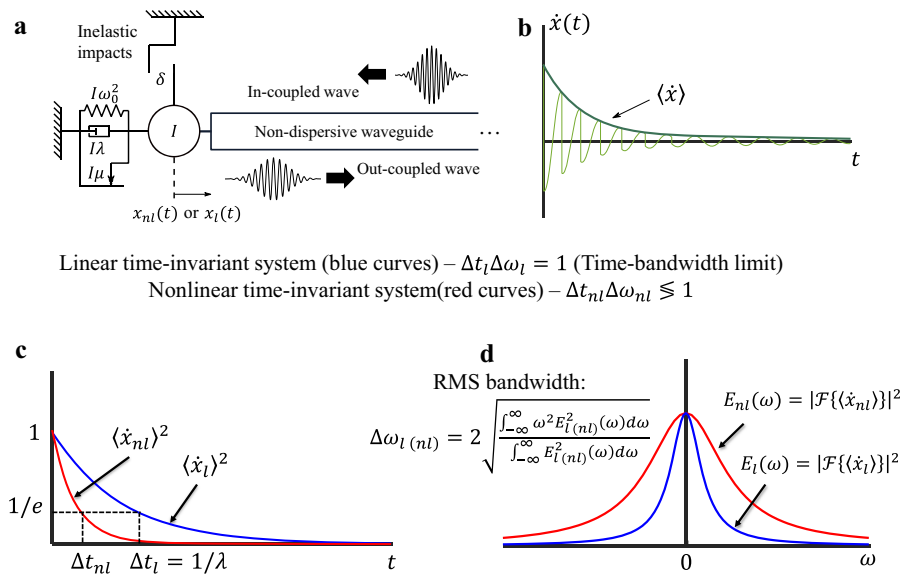


Fig. 1 Scheme for tunable time-bandwidth product in a nonlinear time-invariant system. Basic definitions and the deployed nonlinear time-invariant system are shown: **a** Basic concept of a nondispersive waveguide connected to an oscillator with mass I , linear stiffness coefficient ($I\omega_0^2$), viscous and friction coefficients (λI) and (μI), and linear natural frequency (ω_0). Inelastic impacts [12] occur at a rigid barrier (stop) situated at clearance (δ) from the oscillator. Depending on the occurrence (at higher energy) or absence (at lower energy) of impacts, the oscillator response is denoted by $(x_{nl}(t))$ or $(x_l(t))$, respectively. The temporal (or frequency-domain) difference between the in-coupled and out-coupled waves is solely determined by the response of the oscillator [18] (at their connection point). Hence, the response of only the oscillator suffices for studying the time-bandwidth characteristics of this system. **b** Free response

(velocity, (\dot{x})) of the nonlinear oscillator attached to the waveguide (light green curve), and its envelope ($\langle \dot{x} \rangle$) (dark green curve). **c** Storage time (decay time-constant) of the square of the envelopes of, both, a linear oscillator (in the limit ($\mu = 0, \delta \rightarrow \infty$) – blue curve) whose response is denoted by (x_l) , and a nonlinear oscillator with friction and undergoing inelastic impacts (red curve), similar to the one considered in (a) whose response is denoted by (x_{nl}) . Note that the squared values of the velocity envelopes are considered, since they are proportional to the corresponding total energies. **d** Energy spectral densities of $(\langle \dot{x}_l \rangle)$ and $(\langle \dot{x}_{nl} \rangle)$, that is, $(E_l(\omega))$ (blue curve) and $(E_{nl}(\omega))$ (red curve), respectively, and their associated self-consistent root mean square (RMS) bandwidths [2], $(\Delta\omega_l)$ and $(\Delta\omega_{nl})$

as desired. In our concept (cf. Fig. 1a), a nondispersive acoustic waveguide is rigidly coupled to a SDOF nonlinear oscillator of mass I , stiffness coefficient $\omega_0^2 I$, viscous damping coefficient λI , dry friction coefficient μI , and linear natural frequency ω_0 . The sources of nonlinearity in this system are Coulomb friction (weak nonlinearity), inelastic impacts [12] (strong nonlinearity) of the mass at a rigid barrier (stop) situated at clearance δ , and repulsive magnetic forces when additional magnets are attached to it and to the rigid stop. Depending on the occurrence (at higher energies) or absence (at lower energies) of impacts, the oscillator response is denoted by $x_{nl}(t)$ or $x_l(t)$, respectively.

In this system, it may readily be proved that the difference between the in-coupled waves (i.e., incident waves from the waveguide to the resonator) and out-coupled waves (i.e., outgoing waves from the

resonator to the waveguide) is only affected by the response of the oscillator [21]; hence, it suffices to examine only the dynamics and time-bandwidth characteristics of the nonlinear oscillator itself. Such a system enables us to disproportionately decrease (increase) its decay-time constant (storage time), Δt , compared to a corresponding increase (decrease) of its bandwidth $\Delta\omega$ (cf. Fig. 1b–d) to achieve a time-bandwidth product $(\Delta t \Delta\omega)$ with values either above or below unity ($\Delta t \Delta\omega \leq 1$).

3.1 Experimental fixture assembly

The experimental fixture consists of a pendulum made of a 1/4-in diameter wound carbon fiber composite rod, 45-in long, which is bonded at one end to a 2-in diameter ASTM 306 stainless steel ball of Rockwell hardness C25. The pendulum is then rigidly attached

to a ¼-in diameter (horizontal) ASTM 306 stainless steel rod, 2.5-in long, which acts as a hinge. The hinge is then supported by a pair of SAE 841 bronze flanged oil-embedded sleeve bearings—cf. Fig. 2. For the experiments in which impacts with the rigid barrier (stop) occur, the pendulum ball impacts a $2 \times 5 \times 6$ -in³ steel block supported by a steel vise. The vise is placed so that the impact surface of the steel block is offset 1.18-in from the steel ball and is perpendicular to the plane of motion of the pendulum.

Lastly, for the case where impacts occur in the presence of a magnetic field, i.e., Case 3, the fixture is modified by the addition of two pairs of magnets, 3 inches apart, placed next to the impact surface of the steel block, cf. Fig. 2, and another magnet attached to the bottom of the steel ball of the pendulum. The magnets are placed such that the pairs of magnets on the steel block repel the magnet on the pendulum with the goal of creating an unstable equilibrium point close to and in front of the steel block of the fixture, and, hence, introducing softening nonlinear effects in the dynamics of the pendulum.

Each test was performed as a free-response experiment with non-zero initial angle and zero initial angular velocity. To ensure such initial conditions, the pendulum was held at the desired initial angle by a 12VDC cylinder electromagnet and was released for

each test by cutting the power to the electromagnet. The details of data acquisition and postprocessing are described in the Appendix.

As an experimental realization of the SDOF oscillator of Fig. 1a we have analytically studied, computationally modeled, and experimentally characterized a NTI resonator capable of possessing a time-bandwidth product either *below* or *above* unity. Referring to Fig. 3, the experimental system consists of a pendulum of length L (which is relatively long to achieve slow measured dynamics, i.e., at low frequencies), mass M , moment of inertia I , and natural frequency ω_0 . While at rest, the pendulum mass is situated away from a rigid barrier (stop) at distance δ . Depending on the initial amplitude (energy) of the pendulum, impacts may or may not occur between the pendulum mass and the rigid stop. In this configuration, the sources of energy dissipation are Coulomb friction and viscous damping with coefficients $I\mu$ and $I\lambda$, respectively, originating from the pivot of the pendulum), and, more importantly, the inelastic impacts of the pendulum at the rigid stop. Accordingly, the angle of the pendulum is related to the translational displacement of the oscillator of the model of Fig. 1a simply by $\theta(t) \approx x(t)/L$. A detailed description of the experimental fixture and its mathematical reduced-order model are discussed in the

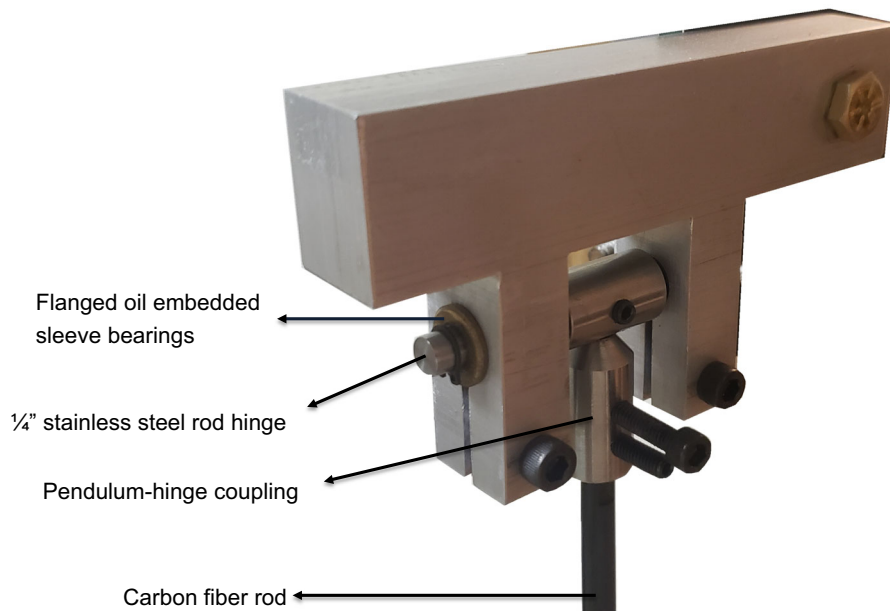


Fig. 2 Configuration of the pendulum mount and pivot. Fully assembled mount of the pendulum, along with the hinge from which it hangs

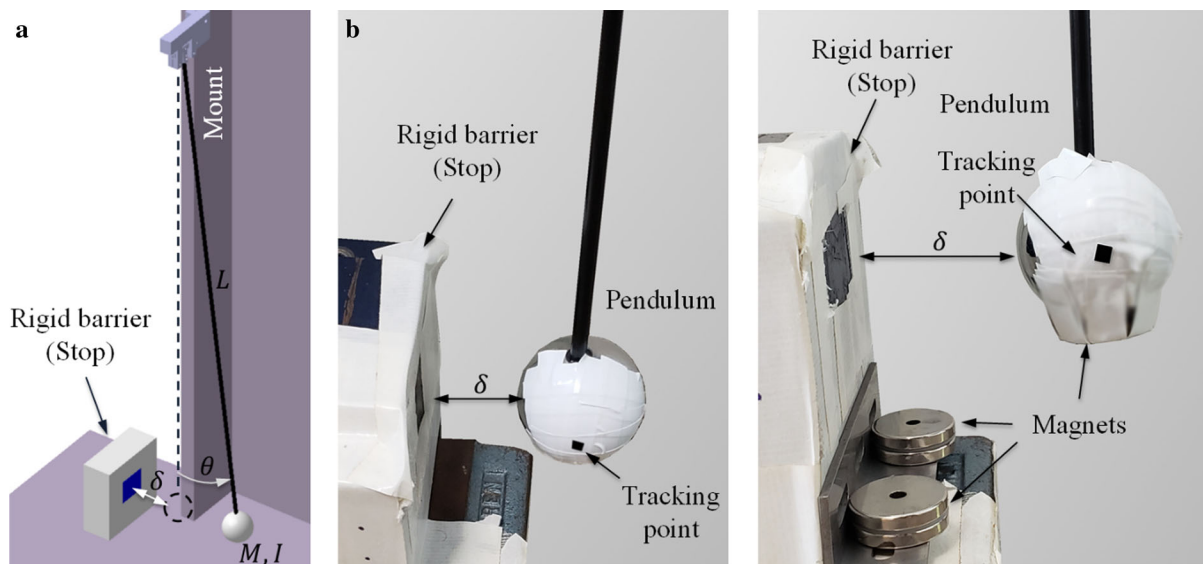


Fig. 3 Experimental configuration. **a** The experimental realization of the oscillator of Fig. 1a consists of a carbon fiber rod of length L (black), a steel ball of mass M attached at the end of the rod (light gray) producing a moment of inertia I , a rigid barrier (light gray), and an impact area (dark blue). **b** Experimental fixture for the considered Case 2, where steel-to-steel inelastic impacts occur—the clearance between the

barrier and the pendulum at rest is equal to δ . **c** Experimental fixture for Case 3, where two pairs of permanent magnets are positioned close to the rigid barrier and an additional magnet is attached to the pendulum mass, generating repulsive magnetic forces between the barrier and the pendulum. These forces are superimposed to the steel-to-steel inelastic impact forces acting on the pendulum mass

next section. At a later phase of the experiments, a set of magnets was attached both at the site of the rigid stop and on the mass of the pendulum giving rise to repulsive magnetic forces between the pendulum and the stop; this arrangement generated softening non-linear forces whose effects on the T-B product we wish to explore. In what follows, we explore the system response in three different configurations, namely where (i) no impacts occur while the system oscillates (case 1); (ii) inelastic impacts occur at the rigid barrier (case 2); and (iii) inelastic impacts occur in the magnetic field generated by the magnets (case 3).

3.2 System identification

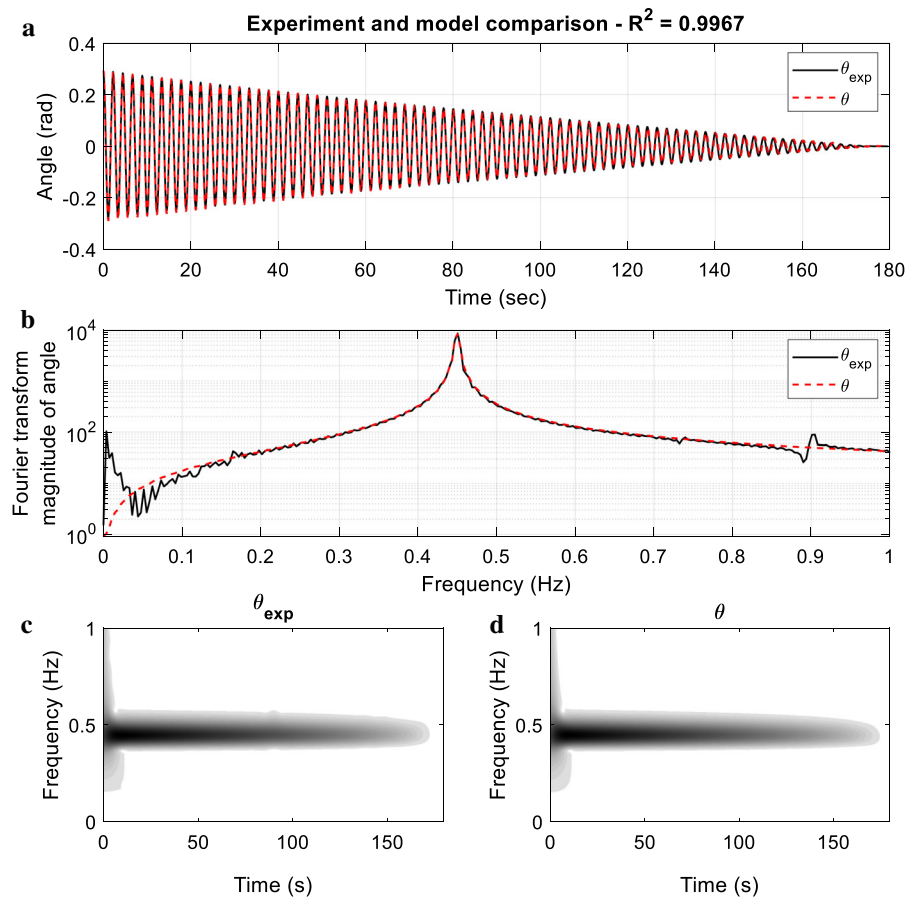
For Case 1 of the experiments, i.e., the case where no impacts occurred, two tests were performed, namely one for system identification and another for validation. For the former, the initial angle was set to $\theta(0) = 6^\circ$, and for the latter to $\theta(0) = 15^\circ$. Due to the presence of friction and the fact that the system was modeled as a single-degree-of-freedom oscillator, we assumed the following reduced-order model for its oscillation,

$$\ddot{\theta} + \lambda \dot{\theta} + \omega_0^2 \theta + \mu \operatorname{sgn}(\dot{\theta}) = 0, \theta(0) = \theta_0, \dot{\theta}(0) = 0, \quad (3)$$

where all coefficients were normalized with respect to the inertia (I) of the pendulum. By performing time series reconciliation, i.e., by matching the experimentally measured time series and the one predicted by the model (3), we obtained the normalized damping coefficient, $\lambda = 0.0056 \text{ s}^{-1}$, natural frequency, $\omega_0 = 2.8247 \text{ rad/s}$, and friction coefficient, $\mu = 0.0056 \text{ rad s}^{-2}$ in (3). Using the identified values, we reproduced the response of the pendulum for the validation experiment with a coefficient of determination [22] of $R^2 = 0.9967$ —cf. Fig. 4. The set of experiments for Case 1 not only allowed us to create an accurate computational model of the pendulum, but also provided the baseline time-bandwidth characteristics based on which we could highlight and assess clearly the effects of the inelastic impacts and the repelling magnetic forces on the said characteristics.

The bandwidth and decay-time constants of this system are shown in Fig. 3a and b, with the time-bandwidth product being normalized by a factor of 1.75 to approach unity for small values of input

Fig. 4 System identification validation. Comparison between **a** the computational reduced-order model (3) (red dashed curve) and the experimental response of the pendulum (black solid curve), showing significant accuracy, i.e., the coefficient of determination [22] is $R^2 = 0.9967$. **b** The corresponding Fourier transform of the time series depicted in **a**. **c** and **d** illustrates the wavelet transform spectra of the response of the experimental response of the pendulum and the identified model (3), respectively



energy. This normalization was performed to better depict and compare the time-bandwidth products of all experimental cases. It should also be noted that for Cases 2 and 3, the corresponding time-bandwidth products were divided by the same normalization factor of 1.75 for fair comparisons with Case 1 and with each other.

Next, we considered Case 2 of our experiments, which is the oscillating pendulum with impact nonlinearity. As explained earlier, the impact nonlinearity is realized by the placing a steel block at a clearance distance of 3 cm from the pendulum. This means that for low enough energies, the oscillations of the pendulum could not overcome that clearance, resulting in behavior analogous to Case 1. For higher energies (larger initial angles) of the pendulum, though, a finite number of inelastic impacts occurred. For this set of experiments, we considered model (3) and updated it to accommodate for the impacts. Each

inelastic impact was modeled using a restitution coefficient, r , less than unity as,

$$-\frac{\dot{\theta}^+}{\dot{\theta}^-} = r < 1, \tag{4}$$

where superscripts in $\dot{\theta}^+$ and $\dot{\theta}^-$ denote the angular velocities before and after the impact, respectively. Considering (4), from our experiments, we were able to compute the restitution coefficient to be $r \approx 0.6$. Therefore, using the identified r and parameters from (3), we could computationally predict the time-bandwidth characteristics of the pendulum with (strong) impact nonlinearity—cf. Fig. 3.

Figure 3a and c illustrates the agreement between the identified model, (3), and the recorded response from the experiment. In the next section, we discuss the direct consequences of the presence of nonlinearity in the dynamics of the pendulum and its time-bandwidth properties.

4 Results

This section considers the time-bandwidth product of the pendulum. Case 1 (no impacts) serves as a baseline to study the effect of energy tunability (nonlinearity) on the time-bandwidth characteristics of such a nonlinear pendulum (oscillator). Initially, the system is set up in such a way that no impacts occur between the oscillator and the barrier, i.e., the considered clearance value δ is large. Hence, the only source of nonlinearity in this case is the weak friction originating in the joints of the experimental fixture, as mentioned before. The time-domain response of the system and its corresponding wavelet transform are shown in Fig. 3a and b, respectively, where we also compare the experimental and corresponding computational (simulation) results of Case 1 (in Fig. 5a)—finding excellent agreement between them. The wavelet transform spectrum in Fig. 5b elucidates the frequency content of the signal. It reveals a fundamental harmonic of constant frequency (~ 0.5 Hz), and additionally, owing to the weak friction nonlinearity, small-amplitude 3rd and 5th harmonics at ~ 1.5 Hz and ~ 2.5 Hz, respectively—both, playing a minor role in the response. Note that, unlike the viscously damped linear oscillator, here, due to the nonlinearity of the system originating from dry (Coulomb) friction, its bandwidth and decay-time constant are energy dependent and tunable. However, as shown from Fig. 4c, even though the system is energy-tunable (nonlinear), its time-bandwidth product does not vary appreciably with respect to the input energy, remaining almost equal to unity throughout—cf. the dash-dotted green curve in Fig. 4c.

For case 2, we set the clearance to $\delta = 3$ cm, so that impacts between the pendulum and the rigid barrier can occur for relatively large input energies. The sharp changes in the velocity signal observed in Fig. 5c and the broadband bright-colored regions in its corresponding wavelet transform spectrum shown in Fig. 5d indicate the occurrence of such impacts. In terms of the dynamics of the system, the impacts cause the system to possess “hardening stiffness nonlinearity” [12], that is, it causes the fundamental frequency of oscillation to decrease with decreasing energy—or, equivalently, increasing time (see inset in Fig. 5d). The impacts release local “bursts” of energy (cf. vertical bright-colored bands in Fig. 5d) resulting, together with the inelasticity of the impacts, in the

energy of the system decreasing after each impact, and giving rise to a multitude of high-frequency harmonics as may be seen in Fig. 5d.

Overall, this intricate phenomenon leads the system to possess much higher dissipative capacity (i.e., higher *bandwidth*, $\Delta\omega$ —cf. red error bars and blue curves in Fig. 4a). Furthermore, the decay-time constant of the system decreases because the hardening nonlinearity increases the frequency of oscillation, thereby increasing the rate of energy dissipated by the damper. Crucially, however, as illustrated in Figs. 1 and 2, the decay rate associated with the generated high harmonics is disproportionately large compared with the decay rate characterizing the fundamental harmonic; overall, this results in the total decay rate (storage time, Δt) to increase (decrease) appreciably more than the aforementioned increase of the bandwidth $\Delta\omega$ of the system—as a result of which the time-bandwidth product, $\Delta t\Delta\omega$, of the system in this case falls *below* unity (see Fig. 6c).

To ensure the accuracy and reproducibility of the measurements and time-bandwidth tunability of the nonlinear system for Case 2, we performed a set of eight tests for each of the initial angles, $\theta_0 = 0.7^\circ, 1.0^\circ, 1.2^\circ, 1.5^\circ, 3.3^\circ, 5.1^\circ, 6.9^\circ, 8.6^\circ, 9.6^\circ$ and 11.2° . For each test, we postprocessed the angular velocity of the system according to what we described before and computed the input energy to the system, bandwidth, decay-time constant, and their normalized product. Finally, we computed the mean value and standard deviation of the eight tests per initial angle and superimposed them onto the time-bandwidth curves in Fig. 6.

Similar to Case 2, in Case 3, we performed eight tests for each of the initial angles $\theta_0 = 1.9^\circ, 2.3^\circ, 2.5^\circ, 2.9^\circ, 3.3^\circ, 4.6^\circ, 6.2^\circ, 6.9^\circ, 8.6^\circ, 9.6^\circ$, and for each experimental test, we computed the time-bandwidth characteristics of the pendulum with impact nonlinearity in the presence of a magnetic force. In Case 3, by contrast, we show that by slightly modifying the experimental configuration of Case 2 we may conceive a dynamical system whose time-bandwidth product can now be energy-tuned to possess values both above *and* below unity. Here, compared to Case 2, we add three sets of magnets, namely two pairs of magnets placed close to the location of the rigid barrier, and an additional magnet directly attached to the mass of the pendulum—cf. Fig. 3, in such a way that the magnets on the barrier repel the magnet on the

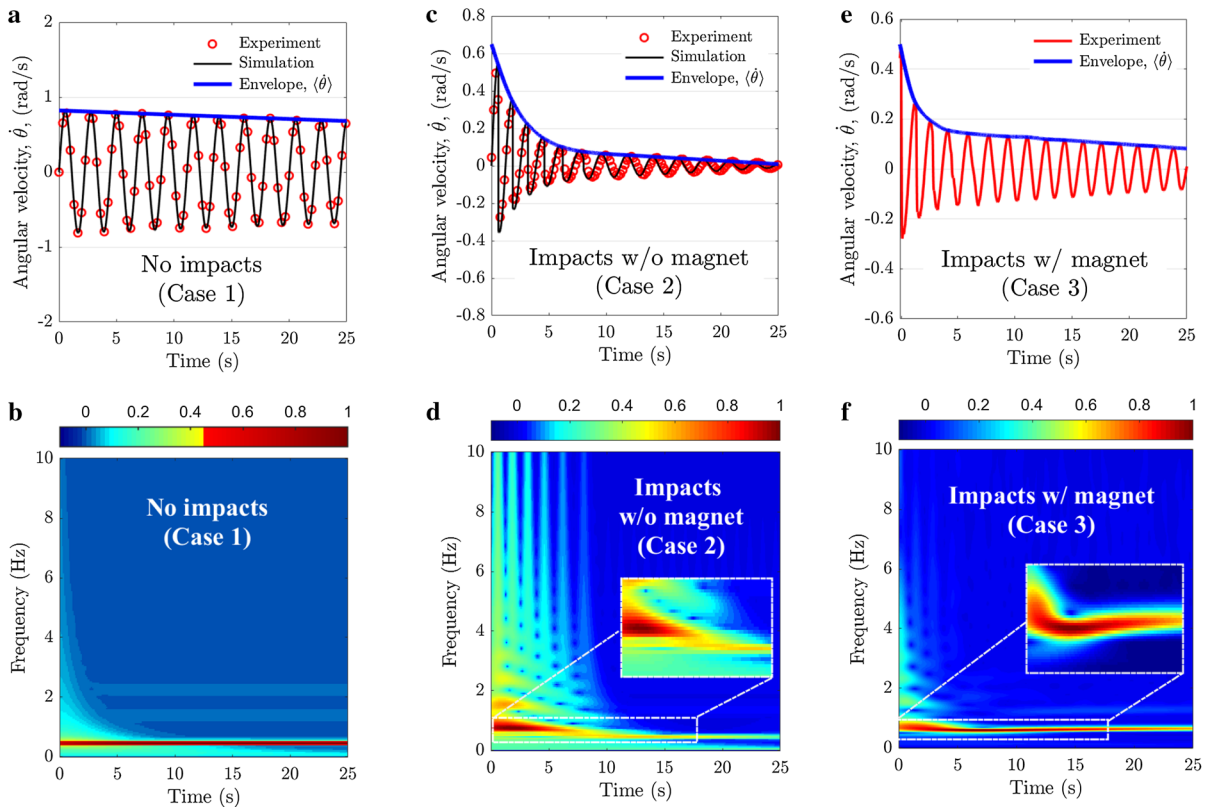


Fig. 5 Angular velocity time series and their corresponding wavelet spectra [7] of the three Cases considered. **a** Simulated angular velocity of the pendulum for Case 1 (no impacts occur) when released from an initial angle of $\theta_0 \sim 15^\circ$ (black curve), along with the corresponding experimental angular velocity of the pendulum (red circles), and their envelope (blue curve). **b** Wavelet transform magnitude (normalized in the range (0,1) by its maximum value), of the experimental response of the pendulum in **a**. **c** Angular velocity of the pendulum for Case 2 (impacts occur) when released from an initial angle of $\theta_0 \sim 11^\circ$

(black curve), along with the corresponding experimental angular velocity of the pendulum (red circles), and their envelope (blue curve). **d** Normalized wavelet transform magnitude of the experimental response of the pendulum in **c**. **e** Experimental angular velocity of the pendulum for Case 3 (impacts occur in the presence of the magnetic field) when released from an initial angle of $\theta_0 \sim 9^\circ$ (red curve), along with its envelope (blue curve). **f** Normalized wavelet transform magnitude of the experimental response of the pendulum in **e**

pendulum. These repulsive magnetic forces introduce a “softening nonlinearity” to the dynamics of the pendulum, whereby its frequency of oscillation increases with decreasing energy, which, in turn, decreases the energy dissipated by the system owing to the reduction of the angular velocity; that is, the decay rate decreases, or the storage time Δt increases—cf. black error bars in Fig. 6b. Simultaneously, as may be seen from Fig. 6a (black error bars), the bandwidth $\Delta\omega$ of the system decreases because the softening nonlinearity decreases the overall energy dissipation of the oscillator—but, crucially, as shown in Figs. 3 and 4, this decrease in $\Delta\omega$ is not so large compared to the increase of the storage time, Δt . Hence, we have the

exact opposite situation to Case 2 (hardening nonlinearity), so the time-bandwidth product $\Delta t \Delta\omega$ characterizing the system may, in this case, exceed unity. For yet higher input energies, the effect of the magnets becomes practically inconsequential, as a result of which we revert, for this system as well, to Case 2, and the T-B product can now also become less than unity.

It is known that nonlinearity (especially stiffness nonlinearity) generates high-frequency harmonics in the time-response of dynamical systems—cf. Fig. 5b, d and f. As a result, the response of, for instance, the pendulum can be expressed as $\dot{\theta}(t) = \sum_{i=1}^{\infty} \dot{\theta}_i(t)$, where $\dot{\theta}_i(t)$ is the component of the angular velocity due to the i -th harmonic. Subsequently, the envelope

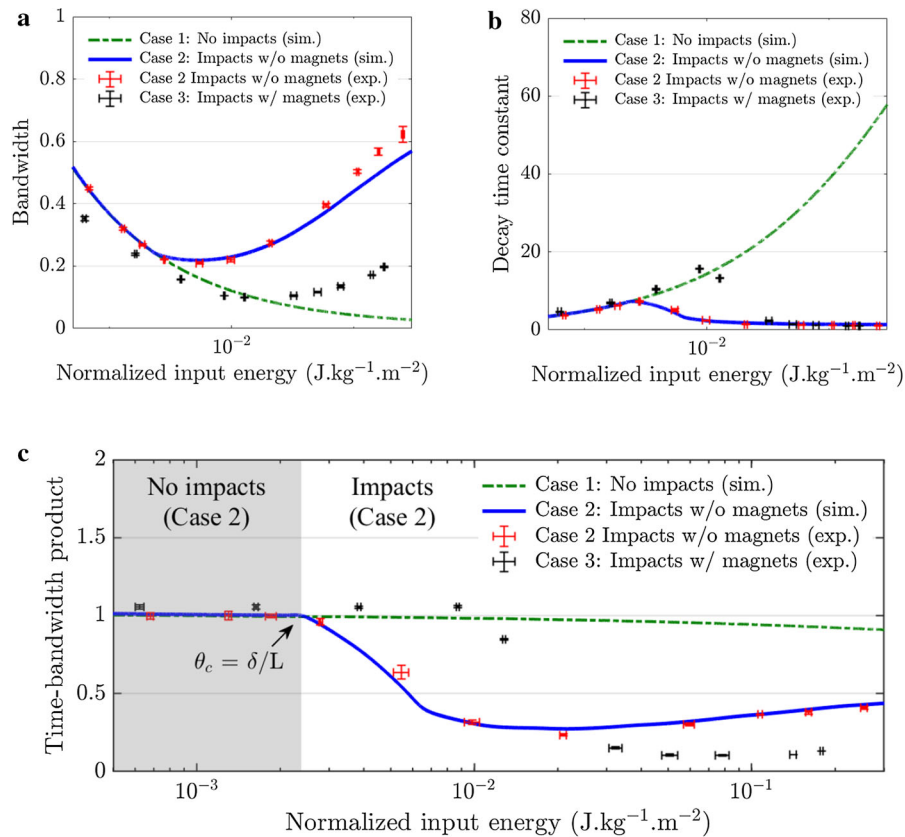


Fig. 6 Time-bandwidth of the nonlinear time-invariant system. **a** Simulated bandwidth of the pendulum without impacts (Case 1) (green curve), and with impacts (Case 2) (blue curve), validated by the corresponding experiments (red error bars). The dissipative capacity (bandwidth) of the system increases compared to Case 1 once the impacts commence. Black error bars represent the experimentally measured bandwidth for Case 3, showing that the softening nonlinearity introduced by the magnetic force *reduces* the bandwidth of the system compared to Case 2. **b** Simulated decay-time constant (storage time) of the system for Case 1 (green curve), along with the simulated and experimental decay-time constant for Case 2 (blue curve and red error bars, respectively) and the experimental decay-time

constant for Case 3 (black error bars). **c** Time-bandwidth product for the cases considered in **a** and **b**. The plots of the time-bandwidth product for Case 1 (simulation: green curve) and Case 2 (simulation: blue curve; experiment: red error bars) show that it goes significantly below unity once the nonlinearity engages ($\theta_0 > \theta_c$), whereas before that it is equal to the time-bandwidth product of the system of Case 1 as expected. Black error bars show that by adding the magnetic field, i.e., the softening nonlinearity, the time-bandwidth product can now be pushed both *above* unity for lower energies and, *below* unity for higher energies once the impacts occur; hence, the tunability with energy of the time-bandwidth product can be proven

of the angular velocity of the pendulum can be expressed as,

$$\langle \dot{\theta}(t) \rangle = \sum_{i=1}^{\infty} \alpha_i \langle \dot{\theta}_i(t) \rangle, \tag{5}$$

where $\dot{\theta}_i(t)$ is the envelope of each harmonic component of the angular velocity, and α_i is associated with the phase difference between the fundamental (1st) and the i -th harmonic of the velocity. Substituting Eq. (5) into Eq. (2), we find that the “nonlinear bandwidth” of

the system, i.e., the bandwidth of the signal $\dot{\theta}(t)$, is given by,

$$\Delta\omega^{*2} = \frac{\sum_{i=1}^{\infty} \alpha_i^4 E_i^2 \Delta\omega_i^{**2}}{E_0^2} + 4 \frac{\int_{-\infty}^{\infty} \left[\omega^2 \left(|\dot{\Theta}|^4 - \sum_{i=1}^{\infty} \alpha_i^4 |\dot{\Theta}_i|^4 \right) \right] d\omega}{E_0^2}, \tag{6}$$

where $(\dot{\Theta} = \mathcal{F}\{\langle \dot{\theta} \rangle\})$, $(\dot{\Theta}_i = \mathcal{F}\{\langle \dot{\theta}_i \rangle\})$, $E_0^2 = \int_{-\infty}^{\infty} |\dot{\Theta}|^4 d\omega$ and $E_i^2 = \int_{-\infty}^{\infty} |\dot{\Theta}_i|^4 d\omega$.

The first term of Eq. (6) includes the contribution of the bandwidth of each harmonic to the bandwidth of the full signal, and the second term represents the contribution due to the interactions between the harmonics. It can be shown that the bandwidth of the full signal is mainly affected by that of the fundamental harmonic and the harmonic interaction term. Depending on the mechanical system, the type of nonlinearity and the coefficients α_i , the computed nonlinear bandwidth can be more, less, or even equal to that of the baseline (approximately linear) system, as can be seen in Fig. 6c. Importantly, it should be noted that due to the fact that the harmonics and their intensities are energy-dependent, the contribution of each term in Eq. (6) varies with energy as well, highlighting the *energy tunability of the bandwidth of the nonlinear system* and the flow of energy in the frequency domain.

The precise mechanism is elucidated with the aid of Figs. 1, 2, 3 and 4. As discussed in the main text, in Case 2, the bandwidth of the system increases, but not by as much as the decay-time constant decreases, so the T-B product becomes less than unity. To demonstrate the significant decrease of the decay-time constant we consider the experimental response associated with an input energy of $\sim 10^{-2} \text{ J kg}^{-1} \text{ m}^{-2}$ and perform inverse wavelet transform harmonic decomposition [23] to separate the fundamental harmonic and the second harmonic (as a representation of all the higher harmonics). The combined response that includes the first and second harmonics and their corresponding wavelet spectra is illustrated in Fig. 7. Comparing the amplitudes of the harmonics with the combined response, the figure indicates that a significant amount of the energy is carried by the second harmonic (and the rest of the higher harmonics). We note that the second and higher harmonics decay at a relatively short time, approximately 5 s, which significantly shortens the decay-time constant (i.e., the storage time). This effect may be further verified by examining the instantaneous decay rates [23] of the fundamental and the second harmonic—cf. Fig. 8. These results show that in addition to rapidly vanishing in ~ 5 s, the second harmonic has a much higher decay rate than the fundamental harmonic (which persists more than 4 times longer compared to the second harmonic), which eventually results in a significant decrease of the overall decay-time constant

of the response of the nonlinear system. We may arrive at the same conclusion by examining the decay-rate of the full signal and its storage time. In cases where the overall decay-rate (mean decay-rate) of the signal after the storage time (since the RMS bandwidth of a system is directly related to its overall decay-rate—in the case of linear systems, bandwidth and decay-rate are equal) is less (greater) than the reciprocal of its storage time ($\Delta\omega \leq 1/\Delta t$), the time-bandwidth product of the system is less (greater) than unity. This interpretation indicates that for systems with time-bandwidth product above (below) unity, the decay-rate of the system increases (decreases) compared to that for time less than the storage time.

The storage time in the case of the signal in Fig. 7a, the mean decay-rate (depicted in Fig. 8) which is 0.24 s^{-1} (where the bandwidth is 0.22), is $\Delta t = 2.4 \text{ s}$ (marked in Fig. 8). In this case, we notice that the mean decay-rate 0.24 s^{-1} is less than the reciprocal of the storage time, $1/\Delta t = 0.42$, of the signal, resulting in time-bandwidth product of less than unity. This means that compared to while the energy of the system reaches 37% of its maximum energy (storage time), the decay-rate of the system decreases.

Next, we turn our attention to Case 3, particularly to the situation corresponding to input energy of $\sim 10^{-2} \text{ J kg}^{-1} \text{ m}^{-2}$ for which the T-B product becomes greater than unity. As stated earlier, in this case, the decay-time constant of the system increases disproportionately compared to how its bandwidth decreases. Again, we explain this with the aid of the instantaneous decay rates of the harmonics. Figure 9 shows the response of the system for the above input energy, its fundamental and second harmonics, and their corresponding wavelet spectra. By comparing the time series of the harmonics, one may observe that the fundamental harmonic loses energy significantly slower than its counterpart in Fig. 7, resulting in an increased decay-time constant. Notably, we see that the amplitude of the second harmonic in the beginning actually *increases*, which contributes to an increase in the storage time. Thus, contrary to Case 2, the 2nd harmonic (and the remaining higher harmonics), instead of more rapidly dissipating the energy of the system, actually stores the energy of the system for longer times. This is further verified by examining the decay rate of the fundamental and the second harmonics (Fig. 10), from which we observe that,

Fig. 7 Harmonic separation—Case 2. Response of the experimental system excited by normalized input energy of $\sim 10^{-2} \text{J kg}^{-1} \text{m}^{-2}$ in **a** the time domain and **b** with its corresponding wavelet spectrum. **c** and **d** show the time series and the wavelet spectrum of the fundamental harmonic, respectively. **e** and **f** show the time series and the wavelet spectrum of the second harmonic, respectively

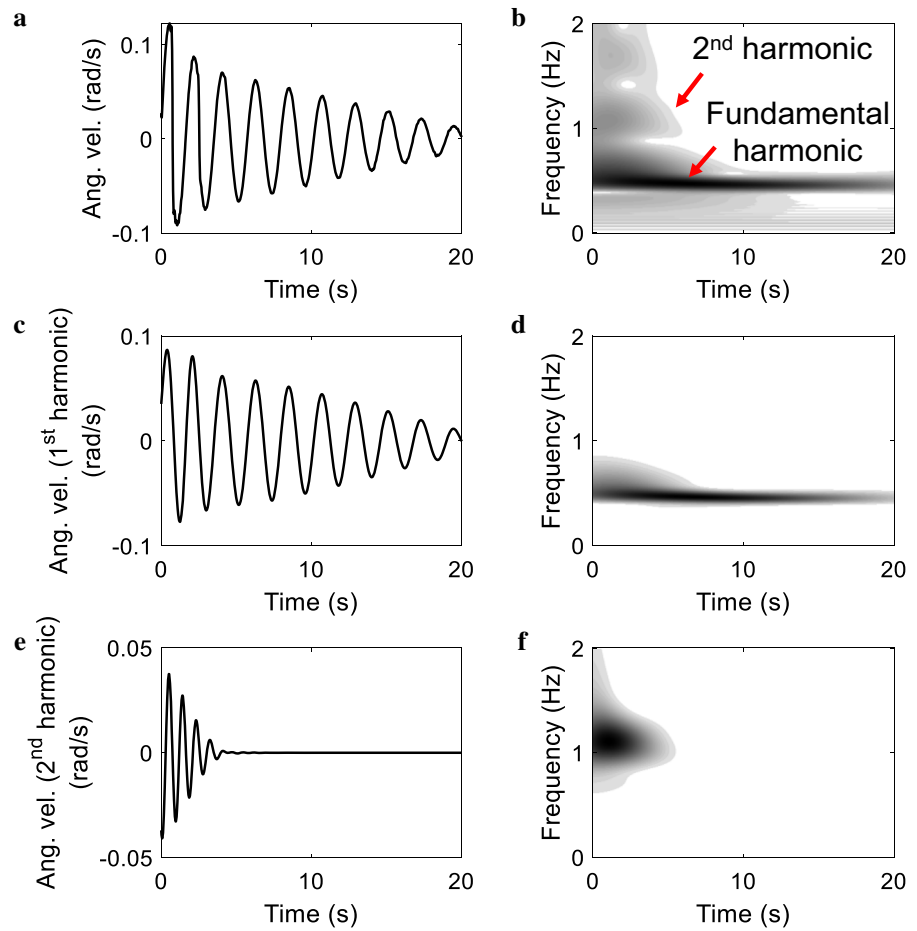


Fig. 8 Decay rates of harmonics—Case 2. The black, the red and the blue curves represent the instantaneous decay rate of the full signal, fundamental and second harmonic, respectively, of the experimental measurements depicted in Fig. 7

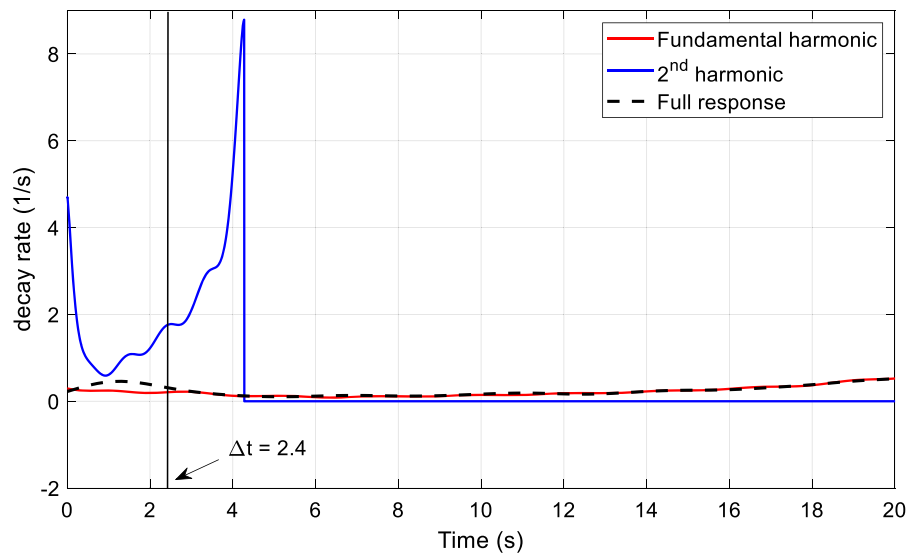


Fig. 9 Harmonic separation—Case 3. Response of the experimental system excited by normalized input energy of $\sim 10^{-2} \text{J kg}^{-1} \text{m}^{-2}$ in **a** the time domain and **b** with its corresponding wavelet spectrum. **c** and **d** show the time series and the wavelet spectrum of the fundamental harmonic, respectively. **e** and **f** show the time series and the wavelet spectrum of the second harmonic, respectively

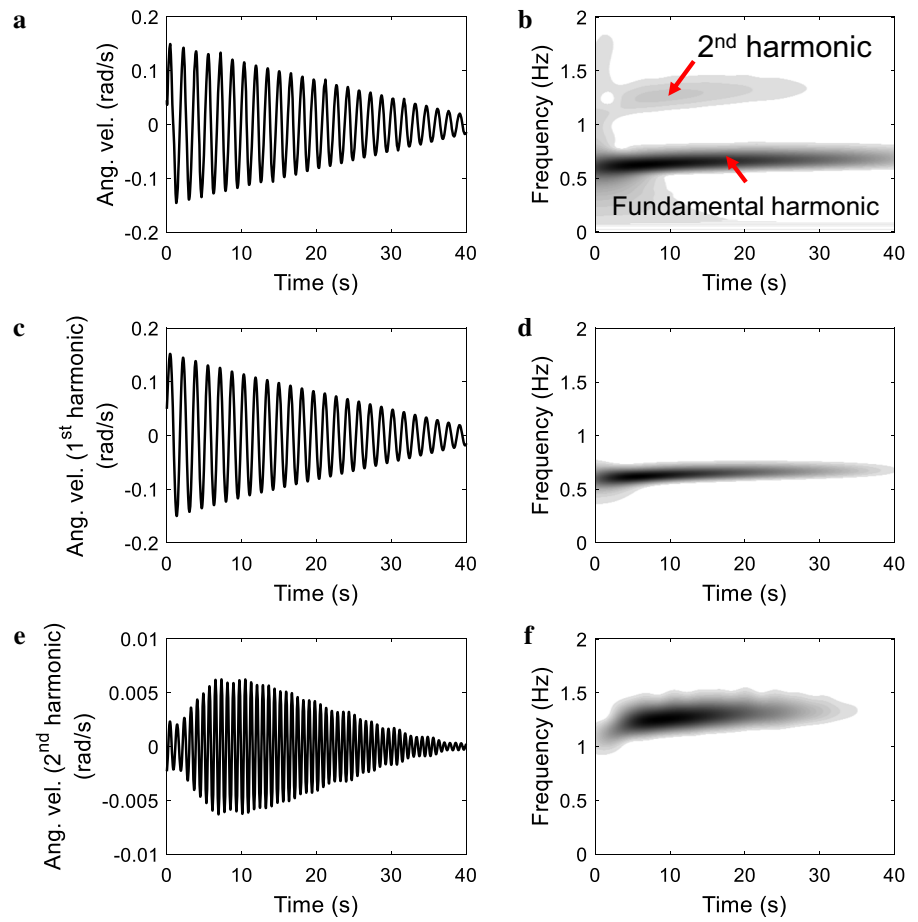
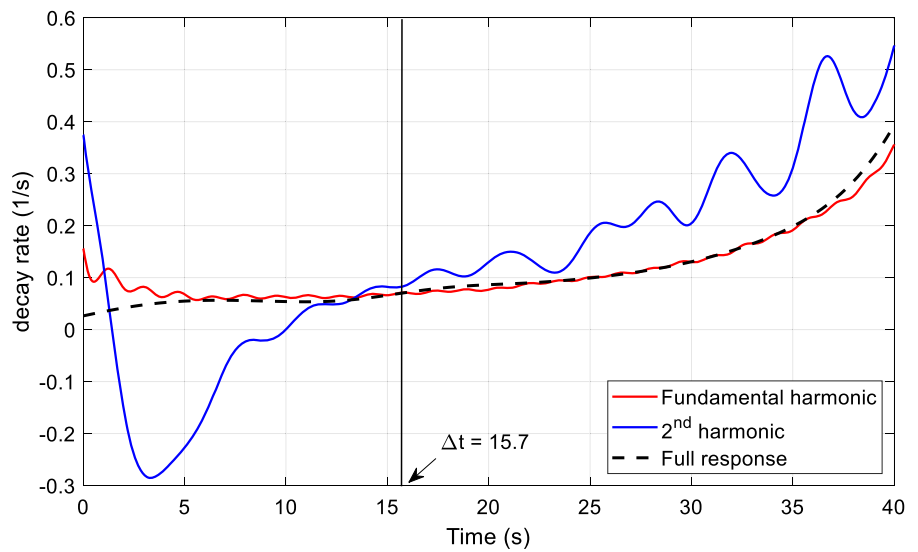


Fig. 10 Decay rates of harmonics—Case 3. The black, the red and the blue curves represent the instantaneous decay rate of the full signal, fundamental and second harmonic, respectively, of the experimental measurements depicted in Fig. 9



unlike the decay rate of the fundamental harmonic that is always positive (meaning that it continuously loses energy), the decay rate of the second harmonic attains negative values at early times during which it actually gains energy; this implies that the second harmonic loses (transfers) energy to the fundamental harmonic. Overall, this nonlinear energy flow mechanism between the harmonics leads to a significant increase in the decay-time constant of the system in Case 3. Examining the mean decay-rate, 0.18 s^{-1} (cf. Fig. 10), and the storage time, $\Delta t = 15.6 \text{ s}$ (marked in Fig. 10) for this case (cf. the full response in Fig. 5a), we see that the mean decay-rate is greater than the storage time reciprocal, implying a time-bandwidth product greater than unity. This means that compared to the time where the system loses 63% of its energy (storage time), the decay-rate of the system increases significantly.

All of the above properties can be physically justified by examining the wavelet transform spectra of the responses of this system (Fig. 5e and f), as well as the dynamics of each harmonic (Figs. 9 and 10) for different ranges of energy, that is, for different times. From Fig. 5e, we discern that at early times, i.e., for high energies, the dynamics is dominated by the hardening nonlinearity (similar to Case 2) caused by the impacts, as the frequency decreases with time in that regime (Fig. 5f up to $\sim 6 \text{ s}$). However, after $\sim 6 \text{ s}$, as explained above, the dynamics is anticipated to be (and in fact is) dominated by the softening nonlinearity because no impacts occur thereafter, since the only source of nonlinearity affecting the oscillation of the system is the softening magnetic forces. As time lapses further, even the softening nonlinear effects die out, and the oscillation frequency becomes almost constant—in that regime, the dynamics is dominated solely by the weak frictional nonlinearity of the system. These effects can also be clearly seen by examining the dynamics of, e.g., the two leading harmonics of the system (Fig. 9). For instance, for the softening regime of Case 3 (between ~ 6 and $\sim 15 \text{ s}$ in Fig. 5f), we see from Fig. 9 that the lifetimes of the harmonics *increase* compared to the same harmonics of Case 2 (Fig. 7), leading to an overall increased storage time Δt , which, combined with the slight decrease in the bandwidth of the system $\Delta\omega$ owing to the nonlinearity, ultimately leads to T-B product above unity, as shown in Fig. 6c (black error

bars). Similar conclusions can be drawn for all other points corresponding to Case 3 in Fig. 6c, by examining the temporal evolution of the corresponding harmonics. The configuration considered in Case 3 allows for more flexibility and tuning (with energy) of the T–B product of the system, both above and below unity. When the input energy is high enough for impacts to occur (i.e., larger than the “critical” energy of $\sim 10^{-2} \text{ J kg}^{-1} \text{ m}^{-2}$), the T–B product of the system is less than unity, as explained above. However, when the same system is excited with input energy less than the critical value, its T–B product becomes larger than unity, owing to the softening nonlinear effects outlined earlier. Finally, the T–B product approaches unity as the input energy decreases even further and reaches a nearly linear regime (with small perturbations provided by friction at the pivot).

5 Conclusion

This work demonstrates experimentally and theoretically that the T–B product of NTI systems can attain values both above and below the classical limit of unity. The key element to achieving this result was to judiciously engineer the nonlinear flow of energy in the frequency domain (through the harmonics generated by the nonlinearity) in a tunable (with energy) way for this system. In fact, for a general class of suitable NTI systems and for sufficiently high excitation intensities (which are needed to trigger nonlinear effects), one may exploit hardening nonlinearities to make the lifetime of the harmonics decrease faster than the increase of the bandwidth of the system, leading to the T–B product falling below unity. By contrast, for smaller energies, one may exploit softening nonlinearities where the opposite effect occurs, namely the lifetime of the harmonics increases faster than the decrease of the bandwidth of the system, leading to the T–B product exceeding unity. Hence, our results open the possibility of conceiving resonant time-invariant systems—ubiquitous throughout wave physics and engineering [9, 24]—where we could harness, in a tunable way, the “benefits of both worlds.” That is, devices that store waves for, simultaneously, long times and broad bandwidths, or resonators with simultaneously broadband resonances with low dissipation rates (or high Q-factors), with a

plethora of hitherto unattainable opportunities for stronger wave-matter interactions, and for buffering, processing and harnessing various types of waves and vibrations.

Funding The authors have not disclosed any funding

Data availability Data will be made available on reasonable request.

Declarations

Conflict of interest The authors declare no conflict of interest.

Appendix: Data acquisition and postprocessing

Due to the very low frequency of oscillation of the pendulum, i.e., ~ 0.5 Hz, typical accelerometers and vibrometers cannot be used to accurately measure its response. For this reason, we recorded (video-captured) the motion of the pendulum at 240 frames-per-second with full HD quality until it settled to its fixed point. For the purpose of tracking the motion of the pendulum, we covered the steel ball with white tape, placed a small black tracking point on it (cf. Fig. 3b and 3c), and filmed its motion at a 14-inch offset from the pendulum. After a video is recorded, we converted it to a series of gray-scale frames to speed up the data acquisition process. To decrease the noise from the capture, we placed a 60×60 pixel moving window on the tracking point to which we then applied a 2D smoothing Gaussian filter with standard deviation of 2. Once the motion of the pendulum is quantified, the coordinate system was placed at its fixed point and, considering the length of the pendulum, its pixel location was converted to an angle. To calculate the angular velocity, we differentiated the time series of the angle time series and suppressed the noise caused by numerical differentiation with a 3rd order lowpass Butterworth filter with cutoff frequency of 10 Hz. Finally, the angular acceleration was obtained by differentiating the filtered angular velocity.

Furthermore, to obtain the envelope of the angular velocity signal, we computed its absolute value and extracted its local maxima, which were at least 0.75 s apart, and assumed values of at least 0.01 rad/s. Then, to obtain the envelope signal, the local maxima were interpolated by Akima Spline curves [25] to avoid extreme fluctuations and ensure C^1 continuity and then

were extrapolated to time $t = 0$ at the left and to the right until the envelope became zero. Once the envelope of the angular velocity signal was obtained, one could compute the bandwidth, decay-time constant, and time-bandwidth product of the system associated with the specific input that produced the angular velocity signal.

References

1. Tsakmakidis, K.L., Shen, L., Schulz, S.A., et al.: Breaking Lorentz reciprocity to overcome the time-bandwidth limit in physics and engineering. *Science* **356**, 1260–1264 (2017)
2. Amoroso, F.: The bandwidth of digital data signal. *IEEE Commun. Mag.* **18**, 13–24 (1980)
3. Chaplain, G.J., De Ponti, J.M., Aguzzi, G., et al.: Topological rainbow trapping for elastic energy harvesting in graded su-schrieffer-heeger systems. *Phys. Rev. Appl.* **14**, 054035 (2020)
4. Fernandes, D.E., Silveirinha, M.G.: Topological origin of electromagnetic energy sinks. *Phys. Rev. Appl.* **12**, 014021 (2019)
5. Guglielmon, J., Rechtsman, M.C.: Broadband topological slow light through higher momentum-space winding. *Phys. Rev. Lett.* **122**, 153904 (2019)
6. Lu, C., Wang, C., Xiao, M., et al.: Topological rainbow concentrator based on synthetic dimension. *Phys. Rev. Lett.* **126**, 113902 (2021)
7. Mojahed, A., Bunyan, J., Tawfick, S., et al.: Tunable acoustic nonreciprocity in strongly nonlinear waveguides with asymmetry. *Phys. Rev. Appl.* **12**, 034033 (2019)
8. Tsakmakidis, K.L., Boardman, A.D., Hess, O.: ‘Trapped rainbow’ storage of light in metamaterials. *Nature* **450**, 397–401 (2007)
9. Tsakmakidis, K.L., Hess, O.: Extreme control of light in metamaterials: complete and loss-free stopping of light. *Phys. B* **407**, 4066–4069 (2012)
10. Tsakmakidis, K.L., Hess, O., Boyd, R.W., et al.: Ultraslow waves on the nanoscale. *Science* **358**, eaan5196 (2017)
11. Tsakmakidis, K.L., You, Y., Stefański, T., et al.: Nonreciprocal cavities and the time-bandwidth limit: comment. *Optica* **7**, 1097–1101 (2020)
12. Vakakis, A.F., Gendelman, O.V., Bergman, L.A., et al.: *Nonlinear Targeted Energy Transfer in Mechanical and Structural Systems*. Springer, Netherlands (2008)
13. Wang, C., Kanj, A., Mojahed, A., et al.: Experimental landau-zener tunneling for wave redirection in nonlinear waveguides. *Phys. Rev. Appl.* **14**, 034053 (2020)
14. Wang, H., Wang, Z., Li, H., et al.: Signal evolution of an optical buffer based on the nonreciprocal silicon-on-insulator waveguide. *Opt. Commun.* **474**, 126158 (2020)
15. Xu, J., Shen, Q., Yuan, K., et al.: Trapping and releasing bidirectional rainbow at terahertz frequencies. *Opt. Commun.* **473**, 125999 (2020)
16. Born, M.: Bemerkungen zur statistischen deutung der quantenmechanik. In: Werner Heisenberg und die Physik

- Unserer Zeit, pp. 103–118. Vieweg+ Teubner Verlag, Wiesbaden (1961)
17. Gasparian, V., Ortuño, M., Schön, G., et al.: Chapter 11 - tunneling time in nanostructures. In: Nalwa, H.S. (ed.) Handbook of Nanostructured Materials and Nanotechnology, pp. 513–569. Academic Press, Burlington (2000)
 18. Gabor, D.: Theory of communication. Part I: the analysis of information. J. Inst. Electr. Eng.-Part III: Radio Commun. Eng. **93**, 429–441 (1946)
 19. Hill, M.: The Uncertainty Principle for Fourier Transforms on the Real Line. University of Chicago, Chicago (2013)
 20. Sapsis, T.P., Dane Quinn, D., Vakakis, A.F. et al. (2012) Effective stiffening and damping enhancement of structures with strongly nonlinear local attachments. J. Vib. Acoust. **134**
 21. Rao, S.S.: Vibration of Continuous Systems. Wiley, New Jersey (2019)
 22. Devore, J.L.: Probability and Statistics for Engineering and the Sciences. Cengage learning, US (2011)
 23. Mojahed, A., Bergman, L.A., Vakakis, A.F.: New inverse wavelet transform method with broad application in dynamics. Mech. Syst. Signal Process. **156**, 107691 (2021)
 24. Gardes, F.Y., Tsakmakidis, K.L., Thomson, D., et al.: Micrometer size polarisation independent depletion-type photonic modulator in Silicon On Insulator. Opt. Express **15**, 5879–5884 (2007)
 25. Akima, H.: A new method of interpolation and smooth curve fitting based on local procedures. J. ACM **17**, 589–602 (1970)

Publisher's Note Springer Nature remains neutral with regard to jurisdictional claims in published maps and institutional affiliations.